

**FuelCell2010-33341**

## MODELING AND SIMULATIONS OF PEMFCs OPERATING WITH PERIODICALLY PURGED DEAD-ENDED ANODE CHANNELS

**Jason B. Siegel**  
University of Michigan  
Ann Arbor, MI, USA

**Anna G. Stefanopoulou**  
University of Michigan  
Ann Arbor, MI, USA

**Serhat Yesilyurt**  
Sabanci University  
Istanbul, Turkey

### ABSTRACT

*PEMFC operation with dead-ended anode has inherent transient behavior: the cell operates between purge cycles that replenish fuel and discharge accumulated gases, such as nitrogen and water vapor, and liquid water. During the operation when the anode exit is shut, gases that cross-over from the cathode accumulate and stratify in the anode channels above the liquid water when the gravity is acting in the flow direction. In this work, we present transient two-dimensional along the channel model and simulations of the PEMFC operating with a dead-ended anode. Transport of gas species in flow channels and gas diffusion layers is modeled by Maxwell-Stefan equations. Flow in the channels is modeled by laminarized Navier-Stokes equations, where the inertial terms are dropped from the force balance, but the buoyancy effect due to the variation of the composition of gas mixture is included at the anode side. Flow in the gas diffusion layers is modeled by Darcy's Law. Permeation of nitrogen in the membrane is considered since it can accumulate in the anode as opposed to instant reaction of oxygen (hydrogen) at the anode (cathode) catalyst layer(s). Membrane is considered as a resistance (interface) to transport of water vapor and nitrogen. Ohm's Law is used to model the transport of charged particles, i.e. electrons in the electrodes and flow plates and protons in the membrane. Finite-element representation of the governing equations in the 2D PEMFC geometry and subject to boundary conditions mimicking experimental conditions is solved using a commercial multiphysics software, COMSOL. According to model results reversible voltage degradation between purge cycles is mostly due to nitrogen accu-*

*mulation in the anode that leads to partial fuel starvation in the cell.*

### INTRODUCTION

To improve the fuel utilization of PEMFCs one has to implement mechatronic solutions with expensive hydrogen grade components and hardware on the anode side, which add cost and complexity to overall balance of the plant. Alternatively, anode side of the PEMFC can be operated at the dead-ended mode with periodic brief purges of dry H<sub>2</sub>, using a pressure regulator instead of mass flow controllers [1,2,3]. There are major drawbacks of the dead-ended anode (DEA) operation. First, since the fuel that is supplied to the anode is not humidified, membrane humidification depends solely on the water produced in the cathode side. Second, large partial pressure of N<sub>2</sub> in the air supplied to the cathode causes a slow crossover to anode through the membrane. Along with N<sub>2</sub>, water vapor accumulates in the anode as well, partially alleviating the first problem, but contributing to the second one. Accumulation of N<sub>2</sub> and H<sub>2</sub>O vapor in the anode hinders the delivery of H<sub>2</sub> to portions of the active area of the fuel cell near the anode exit. Moreover, at higher current densities and cathode humidification, accumulation of liquid water in the anode-GDL leads to further adverse conditions which render the transport of H<sub>2</sub> more difficult in the anode [2,3,4,5,6]. Lastly, H<sub>2</sub> starvation in the PEMFC operating in the DEA mode leads to degradation of the catalyst support through the carbon corrosion mechanism [7]. Despite all its adverse conditions, DEA mode of the PEMFC is not well understood and a closer look at the transport and degradation mechanisms is necessary.

Here, we present a two-dimensional along the channel and through the GDL time-dependent model of the PEMFC operating in the DEA mode. Proposed model is compared with recent experimental observations [8], and captures the qualitative behavior observed in experiments reasonably well. Both experiments and model results exhibit that transient degradation of the cell voltage in the DEA mode is double-sloped: a slow degradation followed by a rapid one. First, H<sub>2</sub> depletion in the anode, which due to the accumulation of N<sub>2</sub>, leads to slow cell voltage decay. When H<sub>2</sub> is completely depleted near the exit portion of the channel, current generating reaction in the cell is limited to the part of the active area that is exposed to sufficient H<sub>2</sub> for the anode reaction. Thus, the local current density in shrinking effective active area increases to match the load current, and results in increasing cathode over potential, and decreasing cell voltage at a faster rate.

In what follows, a description of the 2D model equations, boundary conditions and constraints are presented. Following the description of the model, details of the numerical implementation are presented. Lastly, steady-state and transient simulation results are presented along with a brief discussion.

## DESCRIPTION OF THE MODEL

Figure 1 displays the two-dimensional section of the PEMFC that is used to study variations in species concentration, current density and flow in along the channel and through the GDL directions. The membrane and catalyst layers are very thin and modeled as resistances because of their negligible reservoir effect in long transients of the DEA operation of the PEMFC. Geometric parameters and values of the PEMFC section are listed in Table 1.

**Table 1: Geometric properties of the two-dimensional PEM fuel cell section**

Geometric property	Value
Anode and cathode gas flow channel heights	{2,1} mm
Anode and cathode gas flow channel lengths	73 mm
Anode and cathode gas diffusion layer thicknesses, $\delta_{GDL}$	0.3 mm
Membrane thickness, $\delta_m$	0.025 mm

## Governing Equations

### Transport of gas species

Maxwell-Stefan equations are used for modeling the transport of H<sub>2</sub>, N<sub>2</sub> and H<sub>2</sub>O vapor in the anode channels and GDL, and O<sub>2</sub>, N<sub>2</sub> and H<sub>2</sub>O vapor in the cathode channels and GDL:

$$\frac{\partial}{\partial t}(\rho w_i) + \nabla \left[ -\rho w_i \sum_{j=1}^N D_{ij} \left\{ \nabla x_j + (x_j - w_j) \frac{\nabla p}{p} \right\} + \rho w_i \mathbf{u} \right] = 0 \quad (1)$$

In (1),  $w_i$  and  $x_i$  are the mass and molar fraction of the  $i^{\text{th}}$  species respectively,  $i$  is {H<sub>2</sub>,N<sub>2</sub>,H<sub>2</sub>O} on the anode side, and {O<sub>2</sub>,H<sub>2</sub>O,N<sub>2</sub>} on the cathode side;  $\rho$  is the density of the mixture;  $D_{ij}$  is the binary diffusion coefficient of species  $i$  and  $j$ , which is replaced by the effective coefficient,  $D_{ij}^{\text{eff}} = D_{ij} \varepsilon_g^{1.5}$  in GDLs having porosity of  $\varepsilon_g$ ;  $p$  is pressure, which is assumed to be constant (inlet pressure) as small pressure gradients in GDLs are negligible compared to the concentration gradients; and lastly  $\mathbf{u}$  is the convective (superficial) velocity field, which is calculated by Darcy's Law in the GDLs and by Navier-Stokes equations in the channels. Binary diffusion coefficients in mixtures are determined from [9]:

$$D_{ij} = 3.16 \times 10^{-8} \left( \frac{T^{1.75}}{p(v_i^3 + v_j^3)^2} \right) \left( \frac{1}{M_i} + \frac{1}{M_j} \right)^{1/2} \quad (2)$$

where,  $v_i$  is the molar volume of species  $i$ ,  $T$  is temperature, and  $M_i$  is the molecular weight of species,  $i$ . In the inlet portion of the anode channel (see Fig. 1), the gas diffusivities are scaled with a factor of  $f_{D,in}$  to account for the length and restricted of the gas delivery system and anode inlet plenum. In effect, this factor ensures to limit the back diffusion of anode gasses other than H<sub>2</sub>. Similarly, in the GDLs effective diffusivities are scaled with a factor,  $f_{D,GDL}$ , in lieu of the observations of Fluckiger et al [10], regarding the deviations from the Bruggeman factor especially for cloth GDL materials.

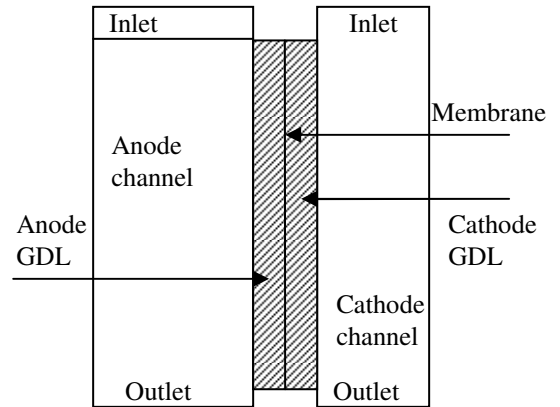


**Figure 1: Layout of the PEMFC section (not-to-scale).**

## Momentum transport

In the anode and cathode GDLs, flow of the gas mixture is modeled as flow through the porous media to calculate the superficial velocity of gas mixtures as follows:

$$\mathbf{u} = -\frac{\kappa_{GDL}}{\mu} \nabla p \quad (3)$$

where,  $\kappa_{GDL}$ , is the permeability of the GDL,  $\mu$  is the viscosity of the mixture. The velocity field in gas diffusion layers is subject to continuity equation:

$$\frac{\partial}{\partial t}(\rho \varepsilon_g) + \nabla \cdot \left( -\rho \frac{\kappa_{GDL}}{\mu} \nabla p \right) = 0 \quad (4)$$

The flows in anode and cathode channels are governed by Navier-Stokes equations:

$$\rho_0 \frac{\partial \mathbf{u}}{\partial t} = -\nabla \cdot \left[ p \mathbf{I} + \mu \left( \nabla \mathbf{u} + (\nabla \mathbf{u})^T \right) \right] + \mathbf{g}(\rho - \rho_0), \quad (5)$$

subject to the continuity equation:

$$\frac{\partial \rho_0}{\partial t} + \nabla \cdot (\rho_0 \mathbf{u}) = 0 \quad (6)$$

In (5),  $\rho_0$  is the reference density of the gas mixture,  $p$  is pressure,  $\mu$  is viscosity,  $\rho$  is the actual density of the gas mixture in the channel,  $\mathbf{u}$  is the velocity field, and  $\mathbf{g}$  is the gravity vector. Note that the flow in the anode channel and GDL is assumed to be weakly compressible, with a body force due to density variations, that is modeled by Boussinesq's approximation [9], thus, in effect, the continuity equation in (6) with constant reference density reduces to steady-state. Flow in the cathode channel is assumed to be incompressible.

## Voltage model

For a specified current load, electrode potential is calculated from:

$$V_e = V_{oc} - \Delta V_{con} - \Delta V_{mem} - \Delta V_{solid} - \Delta V_C - \Delta V_A \quad (7)$$

In (7),  $V_{oc}$  is the open circuit potential of the cell,  $\Delta V_{con}$  is the loss of potential due to concentration losses,  $\Delta V_{mem}$  is the resistive potential loss in the membrane (polymer electrolyte),  $\Delta V_{solid}$  is the resistive loss in the solids (electrodes and current plates),  $\Delta V_C$  is the cathode activation loss, and  $\Delta V_A$  is the anode activation loss. Open circuit cell potential is determined from [11]:

$$V_{oc} = 1.23 - 8.3 \times 10^{-4} (T_0 - 298) \quad (8)$$

Concentration overpotential is given by [11]:

$$\Delta V_{conc} = -\frac{RT}{nF} \left[ \ln \left( \frac{c_{O_2}}{c_{O_2}^{ref}} \right)^{\frac{1}{2}} + \ln \frac{c_{H_2}}{c_{H_2}^{ref}} \right] \quad (9)$$

Part of the concentration loss is due to increasing resistance of the electrolyte [12,13]. During the dead-ended operation, as  $N_2$  and water vapor accumulates near the exit of the anode channel (bottom), transport of  $H_2$  to the active region near the exit becomes diffusion limited through the accumulated gasses.

Katsounis et al [13] measured the resistance of the Nafion membranes for small concentrations of  $H_2$ , and observed that membrane conductivity is nearly unaffected for  $H_2$  partial pressures above 4 kPa, and rapidly decreases for concentrations below that level due to reduced concentration of dissolved protons in the aqueous phase in the membrane. Thus, the diminishing ion concentration in the polymer electrolyte membrane leads to additional resistive losses [12]. The effect of the loss of fuel in increasing resistance of the membrane is specified by a factor,  $f_\sigma$ , and included in the membrane resistive loss as follows:

$$\Delta V_{mem} = f_\sigma \sigma_m J_{cell}, \quad (10)$$

where  $J_{cell}$  is the current density distribution of the cell, and  $\sigma_m$  is the ionic conductivity of the membrane [14],

$$\sigma_m = (-0.326 + 0.514 \lambda) \exp \left[ 1268 \left( \frac{1}{303} - \frac{1}{T} \right) \right]; \quad (11)$$

and  $f_\sigma$  is approximated by:

$$f_\sigma = f_{\sigma,0} + (1 - f_{\sigma,0}) \tanh \left( K_\sigma x_{H_2} \right), \quad (12)$$

where parameters  $f_{\sigma,0}$  and  $K_\sigma$  are provided in Table 2.

The ohmic loss in solid conductors is given by:

$$\Delta V_{solid} = V_e - V_{cell} = J_{cell} R_{solid}, \quad (13)$$

where  $R_{solid}$  is the overall resistance [ $\Omega \cdot m^2$ ] of the solid components, and contact between them,  $V_{cell}$  is the cell potential and calculated from the requirement that it has to be constant, because of the high conductivity of the current plate. The distribution of the cell current density is subject to the following constraint:

$$\int_{A_{cell}} J_{cell} dA = J_{load} A_{cell}. \quad (14)$$

Cathode activation overpotential is obtained from the Butler-Volmer expression for the electrode kinetics:

$$\Delta V_C = \frac{RT}{F\beta_c} \operatorname{asinh} \left\{ \frac{J_{cell}}{i_{0,ref}^C} \left( \frac{c_{O_2}^{ref}}{c_{O_2}} \right)^{\gamma_{O_2}} \left( \frac{c_{H^+}^{ref}}{c_{H^+}} \right)^{\gamma_{H^+}} \right\}, \quad (15)$$

where  $\beta_{ca}$  is the transfer coefficient, and  $i_{0,ca}^{ref}$  is the reference exchange current density, and the effect of the proton (reactant) concentration,  $c_{H^+}$ , which is typically neglected in flow-through models, is included on the cathode side.

Similarly to the cathode activation overpotential, anode activation overpotential is given by:

$$\Delta V_A = \frac{RT}{F\beta_A} \operatorname{asinh} \left\{ \frac{J_{cell}}{i_{0,ref}^A} \left( \frac{c_{H_2}^{ref}}{c_{H_2}} \right)^{\gamma_{H_2}} \right\}. \quad (16)$$

In (1), (4), (5), (6), (7) and (14), we have the following unknowns: total of six  $w_i$  for  $i \in \{H_2, N_2, H_2O\}$  on the anode side and  $i \in \{O_2, N_2, H_2O\}$  on the cathode side; anode and cathode GDL pressures; anode and cathode channel velocities and pressures; and the cell voltage,  $V_{cell}$ , which is constant, and the current distribution,  $J_{cell}$ .

Boundary conditions for equations(1), (4), (5) and (6) are specified in what follows.

## Boundary conditions

### For mass transport

At the anode inlet, mass fractions of  $H_2$  and  $N_2$  are specified in flow through simulations; and specified mass fraction of  $H_2$  and insulation boundary condition for  $N_2$  are used in the dead-ended transients. At the cathode inlet, since the cathode is flow through at all times, inlet mass fractions of species are specified based on the relative humidity of the cathode inlet.

At exits of anode and cathode flow channels, for all species convective flux boundary conditions are used:

$$\mathbf{n} \cdot \left[ -\rho_i \sum_{j=i} D_{ij} \nabla x_j \right] = 0. \quad (17)$$

At interfaces between the membrane-catalyst layers and GDLs, total fluxes of species are specified. For reactant gasses,  $H_2$  and  $O_2$  cell current distribution is used to specify the reaction rate:

$$\rho w_i \left[ \mathbf{u} - \sum_{j=i} D_{ij} \nabla x_j \right] \cdot \mathbf{n} = \frac{M_i J_{cell}}{n_i F}. \quad (18)$$

For  $N_2$ , permeation through the membrane is used to specify the flux boundary condition:

$$\begin{aligned} \rho w_{N_2} \left[ \mathbf{u} - \sum_{j=N_2} D_{N_2 j} \nabla x_j \right] \cdot \mathbf{n}^{(A,C)} \\ = \zeta^{(A,C)} M_{N_2} \psi_{N_2} \left( p_{N_2}^C - p_{N_2}^A \right) / \delta_m \end{aligned} \quad (19)$$

where,  $\zeta^{(A,C)}$  is a convenient factor which indicates the direction of the flux, -1 for anode and 1 for the cathode fluxes, and  $\psi_{N_2}$  [mol-m<sup>-1</sup>-s<sup>-1</sup>-Pa<sup>-1</sup>] is the permeance of  $N_2$  through membrane, which depends on the membrane water content and temperature [2,4]:

$$\begin{aligned} \psi_{N_2} = 10^{-4} (0.0295 + 1.21 f_V - 1.93 f_V^2) \times \\ \exp \left[ \frac{E_{N_2}}{R} \left( \frac{1}{303} - \frac{1}{T_0} \right) \right], \end{aligned} \quad (20)$$

In (20),  $E_{N_2}$  is 24kJ-mol<sup>-1</sup>;  $f_V$  is the volumetric ratio of water in the membrane and depends on the number of water molecules per sulfonic group in the membrane,  $\lambda$ :

$$f_V = \frac{\lambda V_{H_2O}}{V_m + \lambda V_{H_2O}}, \quad (21)$$

where  $V_{H_2O}$  and  $V_m$  are molar volumes of water and dry membrane.

Specified flux boundary conditions at the membrane GDL interfaces are also used for  $H_2O$ ; total resistance across the membrane and the electro-osmotic drag terms are implemented. On the cathode side, water vapor flux also includes the cell-current dependent generation term in addition to the resistance and electro-osmotic drag terms:

$$\begin{aligned} \rho w_{H_2O} \left[ \mathbf{u} - \sum_{j=H_2O} D_{H_2O j} \nabla x_j \right] \cdot \mathbf{n}^{(A,C)} = \\ \zeta^{(A,C)} M_{H_2O} \left[ \frac{c_{SO_3}^0 (\lambda_C^* - \lambda_A^*)}{R_{mem}} - \frac{(n_D + \chi^{(A,C)}) J_{cell}}{F} \right], \end{aligned} \quad (22)$$

where,  $\zeta^{(A,C)}$  is defined in (19),  $\chi^{(A,C)}$  is 1/2 for the cathode and 0 for the anode flux, and  $\lambda_{(A,C)}^*$  is the equilibrium concentration of water molecules per sulfonic group on anode and cathode sides respectively and interpolated from the following expressions for the operating temperature [15]:

$$\lambda^* = \begin{cases} 0.043 + 17.81 a - 39.85 a^2 + 36 a^3, & T = 303K \\ 0.3 + 10.8 a - 16 a^2 + 14.1 a^3, & T = 353 K \end{cases} \quad (23)$$

In (22),  $R_{mem}$  is the mass transfer resistance to water transport in the membrane, and given by:

$$R_{mem} = \frac{\delta_m}{D_\lambda} + \frac{1}{k_{des}} + \frac{1}{k_{ads}}, \quad (24)$$

where  $\delta_m$  is the thickness of the membrane,  $D_\lambda$  is the diffusivity of water in the membrane and interpolated from the following expressions for the operating temperature [15]:

$$D_\lambda = 2.72 \times 10^{-9} f_\lambda \exp \left[ 2416 \left( \frac{1}{T} - \frac{1}{T_0} \right) \right] \quad (25)$$

$$f_\lambda = \begin{cases} .0543 + .00336\lambda, & T = 323\text{K} \\ .0771 + .00259\lambda, & T = 353\text{K} \end{cases}$$

In (25),  $k_{i(des,ads)}$  are desorption and adsorption coefficients of the membrane respectively, and given by [15]:

$$k_{ads} = 1.14 \times 10^{-5} f_V \exp \left[ 2416 \left( \frac{1}{T} - \frac{1}{T_0} \right) \right], \quad (26)$$

and

$$k_{des} = 4.59 \times 10^{-5} f_V \exp \left[ 2416 \left( \frac{1}{T} - \frac{1}{T_0} \right) \right]. \quad (27)$$

At solid walls, insulation boundary conditions are used for all species.

### **For momentum transport in GDLs**

Superficial velocities in GDLs are calculated from (3) by solving (4). At GDL-channel interfaces, the pressure is specified as the cell operating pressure for both anode and cathode:

$$p = p_0. \quad (28)$$

At interfaces between GDLs and the membrane, the superficial velocity of the mixture is calculated from the sum of the fluxes of all species defined in (18), (19) and (22). At GDL boundaries near the inlet and outlet, the velocity is set to zero as insulating boundaries.

### **For momentum transport in the channels**

Boundary conditions of the anode channel are specified as constant pressure at the inlet and specified velocity at the exit. For flow through and purge conditions, the exit velocity is non-zero, however for the dead-ended operation the exit velocity is specified as zero. At the anode channel-GDL boundary the normal velocity component is set to the velocity calculated from (3) in the GDL.

For the cathode channel, inlet velocity is specified using the cathode stoichiometric ratio of the flow and the exit is specified as constant pressure. At the cathode channel-GDL boundary no-slip conditions are used, assuming that the cathode flow rates are sufficiently high.

All solid boundaries in both channels are treated as no-slip boundary conditions.

## **Numerical model**

Equations (1), (4) and (5) subject to continuity (6), boundary conditions (17)-(19), (22) and (28) along with insulation and no-slip conditions on the solid walls are solved with finite-element method using a commercial software COMSOL [16]. PEMFC section shown in Fig. 1, is discretized by 6005 second-order Lagrangian rectangular elements with 100,012 degrees of freedom. Constraints given by (7) and (14) are imposed as weak-boundary equations on the membrane interface. Steady-state simulations are started with specified uniform initial conditions, such as inlet mass fractions specified as initial mass fraction of all species, cell pressure for the pressure in GDLs and resting fluid for flow in the channels. Steady-state solutions are either bootstrapped by solving flow in the channels and GDLs, mass fractions of species in anode and cathode, or by restarting from a similar steady-state solution. For the solution of linear system of equations UMFPACK solver is invoked in the code.

Transient simulations are started from steady-state simulations at the given load current density and other operating conditions. For time-integration, variable time-step and up to 5<sup>th</sup> order Backward-Difference Formula are invoked in the code. A typical 1200-second-transient simulation takes about 2000 seconds on the 4-nodes of a dual quad-core 2.6 GHz workstation, and addresses about 1.5 GB of memory.

**Table 2: Parameters used in the model**

Property, symbol	Value*
Porosity of GDLs, $\varepsilon_g$	0.6
Channel inlet diffusivity factor, $f_{D,in}$	0.001
GDL diffusivity factor, $f_{D,GDL}$	1/3
Permeability of GDLs, $\kappa_{GDL}$	$10^{-13}$
Viscosity of gas mixtures, $\mu$	$\{2,2\} \times 10^{-5}$
Anode and cathode transfer coefficients, $\beta_{\{A,C\}}$ [11]	{1,1}
H <sub>2</sub> and O <sub>2</sub> reference concentrations, $c_{\{H_2,O_2\}}^{ref}$	{56,4,40}
Electro-osmotic drag coefficient, $n_d$ [14]	$(2.5/22) \times \lambda$
Concentration of SO <sub>3</sub> in dry membrane, $c_{SO_3}^0$	1200
Density of dry the membrane, $\rho_m$	2020
Molecular weight of the membrane, $M_m$	1.1
Anode and cathode reference current densities, $i_{0,ref}^{(A,C)}$ [tuned]	$3 \times \{10^4, 10^{-2}\}$
Overall electrical resistivity of the cell, $R_{solid}$ [tuned]	$0.4 \times 10^{-4}$ $\Omega \cdot m^2$
Membrane conductivity loss factor limit, $f_{\sigma,0}$	0.01
Membrane conductivity loss factor coefficient, $K_\sigma$	30
H <sup>+</sup> concentration parameter, $\gamma_{H^+}$	1/2
O <sub>2</sub> concentration parameter, $\gamma_{O_2}$	1/2
H <sub>2</sub> concentration parameter, $\gamma_{H_2}$	1/2

\* All units are specified in SI

## RESULTS

### Steady-state flow-through simulations

The model is verified by means of comparing flow through simulations, which correspond to a number of load current densities ranging from 50 A·m<sup>-2</sup> to 12000 A·m<sup>-2</sup>, with the flow through data [8]. Parameters such as the anode and cathode reference current densities and the overall resistance of the solid components and contacts in the cell are tuned to match the flow through data; results are shown in Fig. 2.

### Transient simulations

For the simulation of dead-ended cycles, the transient runs started from the steady-state conditions already attained. It is

assume that the purge conditions would be similar to the steady-state flow through results. Transient simulations of the dead-ended-anode operation of the PEMFC are extremely susceptible to numerical stiffness issues especially towards the end of the cycle when H<sub>2</sub> is severely depleted near the outlet of the channel. In fact, steady-state dead-ended operation could not be achieved for moderate load current densities.

Transient simulations are compared against the data reported in [8] for  $J_{load} = 3770$  and  $5660$  A·m<sup>-2</sup> in Figs. 3 and 4; agreement of the results is only qualitative. Similar to the observations in experiments, double-sloped transient responses of the cell voltage are also observed in the simulations as shown in Figs. 3 and 4.

The change in the slope of cell voltage takes place at  $t \simeq 900$  s in simulations, after which the cell voltage rapidly deteriorates; the time at which the cell voltage drop changes its slope is slightly lower for  $J_{load} = 5660$  than for 3770. Moreover, according to experimental results, the slope changes nearly at  $t \simeq 400$  s for both currents as well. Large discrepancy in the times of the slope changes indicates that the accumulation rate of N<sub>2</sub> is significantly lower in the model, which can be attributed to strong dependence of the N<sub>2</sub> permeance on the water content of the membrane [2,8]. Even if we assume that the N<sub>2</sub> permeance given by (20) is accurate, a small discrepancy between the calculated water content and the actual water content of the membrane in experiments would yield a large discrepancy in the N<sub>2</sub> cross-over rate.

Depletion of H<sub>2</sub> takes place due to accumulation of N<sub>2</sub> and water vapor in the anode. Distribution of H<sub>2</sub> mole fraction in the anode-membrane interface is shown in Fig. 5; in the figure  $y=0$  corresponds to the exit of the channel, and  $y=0.073$  m corresponds to the inlet. At about  $t \sim 1000$  sec, when the rapid deterioration of the cell voltage sets in, the H<sub>2</sub> mole fraction is about zero near the outlet ( $y=0$ ).

In Fig. 6, evolution of the cell current density distribution is shown. The cell current density is almost uniform until when the H<sub>2</sub> mole fraction goes to zero near the outlet of the anode channel (see Fig. 5) at  $t \simeq 1000$  s, after which the current density drops severely near the exit of the channel ( $y=0$ ). To balance the overall load current, the distribution of the cell current density increases near the inlet. When significant portion of the cell begins to operate at a higher current density, the cathode over potential increases; and, hence, the cell potential decreases.

The volume fractions of N<sub>2</sub> and H<sub>2</sub>O vapor accumulating in the anode channel are shown in Fig. 7. Accumulation of N<sub>2</sub> is gradual and does not reach to steady-state in 1200 seconds. On the other hand, water vapor accumulation is fast and reaches to its steady-state at the beginning of the transient, and remains

constant for up to  $t \approx 1000$  seconds. As shown in Fig. 8, water vapor accumulation increases for  $t \gtrsim 1000$ , when the electro-osmotic drag of water from anode to cathode is reduced in portions where the cell current diminishes near the exit of the anode channel.

**Table 3: Base operating conditions**

Property, symbol	Value
Cell operating temperature, $T_0$	338 K
Anode and cathode pressure, $p_0$	125 kPa
Cathode stoichiometric ratio	3
Cathode inlet relative humidity	0.6
Anode stoichiometric ratio (flow through simulations)	0.1
Anode relative humidity	0

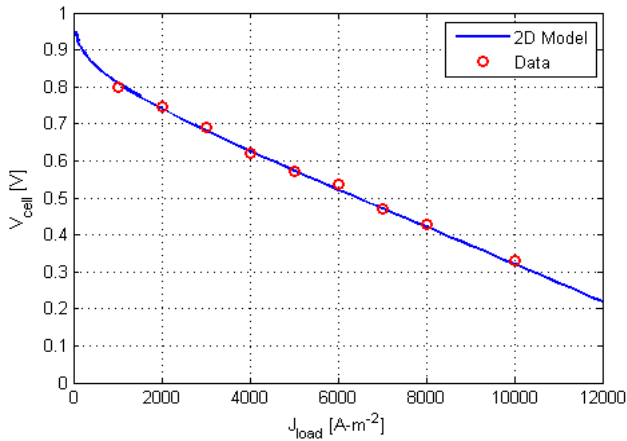


**Figure 2: Polarization curve obtained by the model compared with experimental data.**

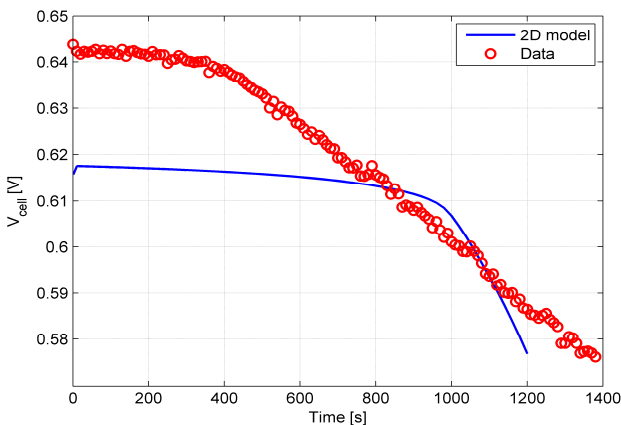


**Figure 3: Transient response of cell voltage when the anode exit is shut off, for  $J_{load} = 3770 \text{ A}\cdot\text{m}^{-2}$ .**

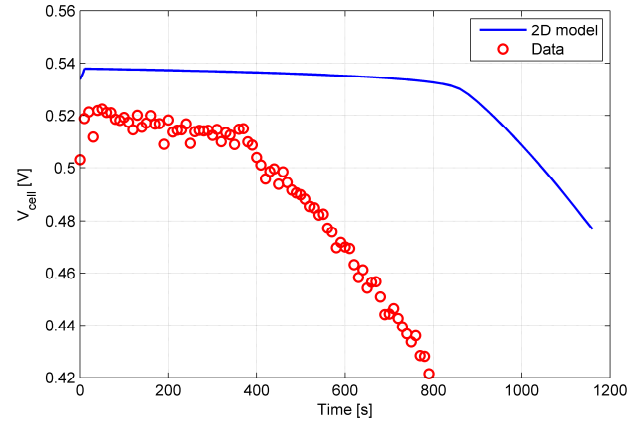


**Figure 4: Transient response of cell voltage when the anode exit is shut off, for  $J_{load} = 5660 \text{ A}\cdot\text{m}^{-2}$ .**

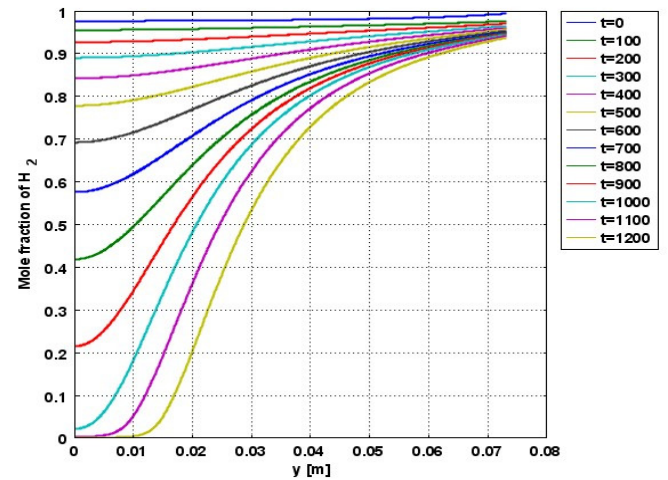


**Figure 5: Evolution of the mole fraction of  $\text{H}_2$  at the membrane interface for  $J_{load} = 3770 \text{ A}\cdot\text{m}^{-2}$ .**

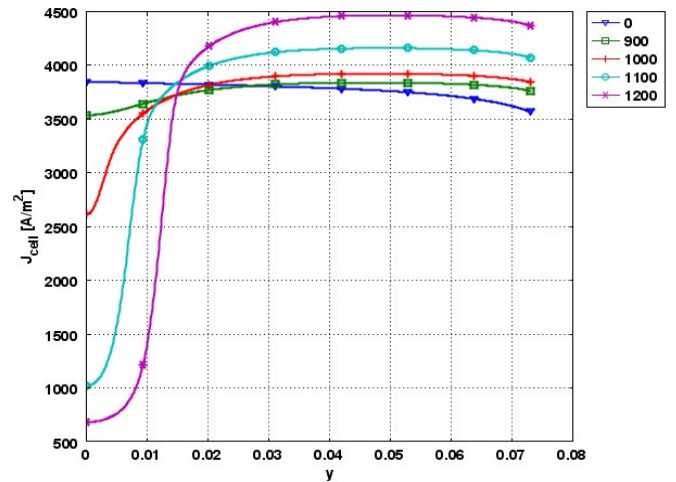


**Figure 6: Evolution of the cell current density distribution for  $J_{load} = 3770 \text{ A}\cdot\text{m}^{-2}$ .**

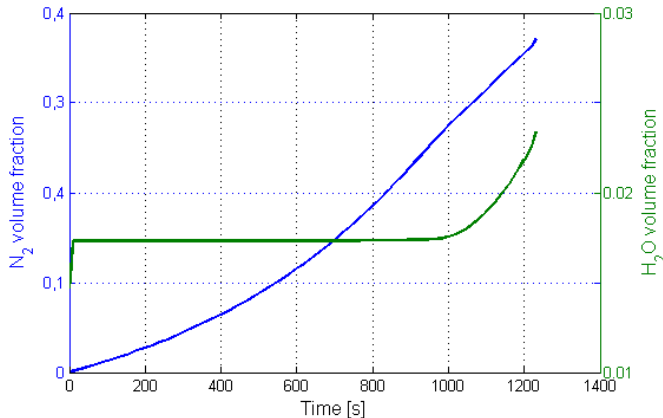


**Figure 7: Volume fraction of  $N_2$  (blue, left axis) and  $H_2O$  vapor (green, right axis) in the anode channel for  $J_{load} = 3770 \text{ A}\cdot\text{m}^{-2}$ .**

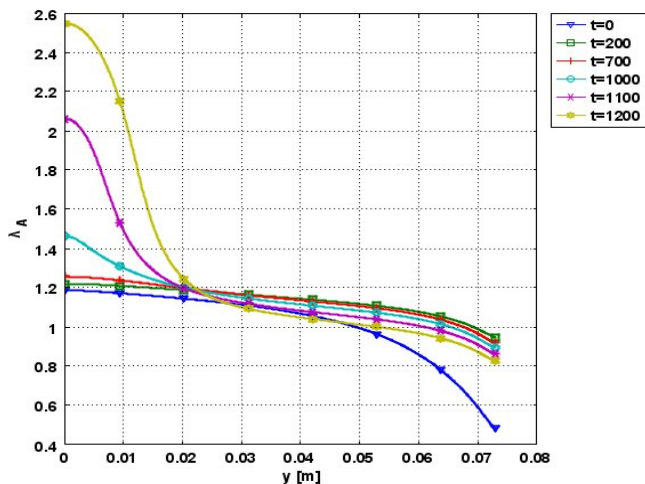


**Figure 8: Evolution of the equilibrium water content of the membrane at the anode-interface for  $J_{load} = 3770 \text{ A}\cdot\text{m}^{-2}$ .**

## CONCLUSIONS

A two-dimensional time-dependent model of the PEMFC operating with dead-ended anode between periodic purges is presented here. In the model, only anode and cathode reference current densities, and overall electric resistance (including contact resistances) are tuned to match the flow through data obtained from the PEMFC.

Two dead-ended transients for different load current densities are simulated and compared with experimental data. In both cases, model results poorly match the cell voltage *vis à vis* albeit with reasonable qualitative agreement. The discrepancy is attributed to the effect of the  $N_2$  permeance through the membrane, which strongly depend on the volume fraction of the water in the membrane. Due to dry operating conditions small dis-

crepancies in the calculated water content of the membrane may yield large discrepancies in the accumulated  $N_2$  in the anode channels.

Model captures the double-sloped-cell-voltage response observed in the experiments well. The time of slope change in deteriorating cell voltage remains nearly the same in the simulations as well in the experimental results. According to results obtained in simulations, the time of slope change coincides with the severe depletion of  $H_2$  near the shut exit of the anode. After that time, active cell area that provides current for the load begins to retreat, and results in increasing local current density in that portion. As the actual current density of the cell in the effective active area increases, increasing cathode over potential results in net decrease in the cell potential.

Unlike  $N_2$ , water vapor accumulation in the anode is fast at the beginning of the transient and remains constant until when the cell current diminishes in  $H_2$  depleted areas. Afterwards, water accumulation speeds up again due to reduced electro-osmotic drag in those parts of the cell.

Moreover, simulation experiments (not shown here) show that the gravity does not play an important role in the accumulation of  $N_2$  and  $H_2O$  vapor near the exit (at the bottom of the anode channels with respect to the orientation of the gravity), where the primary effect is the convective flux of  $H_2$  near the inlet that compensates for the diffusive flux of  $N_2$  and  $H_2O$  as discussed in detail by Siegel *et al* [8].

## ACKNOWLEDGMENTS

This work was supported by The Scientific and Technological Research Council of Turkey, TUBITAK-MAG 109M105, and the National Science Foundation through CBET-0932509.

## REFERENCES

- [1] Karnik, J. Sun, and J. Buckland, 2006, "Control analysis of an ejector based fuel cell anode recirculation system," In Proceedings of American Control Conference, June 2006.
- [2] Ahluwalia, R.K, Wang, X., 2007, "Buildup of nitrogen in direct hydrogen polymer-electrolyte fuel cell stacks," *J. Power Sources*, **171**, pp. 63-71.
- [3] Muller, E.A., Kolb, F., Guzzela, L., Stefanopoulou, A.G., McKay, D., 2010, "Correlating nitrogen accumulation with temporal fuel cell performance," *J. Fuel Cell Science and Technol.*, **7**(2):021013.
- [4] Kocha, S.S., Yang, J.D., Yi, J.S., 2006, "Characterization of gas crossover and its implications in PEM fuel cells," *AICHE Journal*, **52**(5), pp. 1916-1925.
- [5] Weber, A.Z., 2008, "Gas-crossover and membrane-pinhole effects in polymer electrolyte fuel cells," *J. Electrochem Soc.*, **155**(6), pp. B521-B531.
- [6] Siegel, J.B., McKay, D.A, Stefanopoulou, A.G., Hussey, D.S., Jacobson, D.L., 2008, "Measurement of liquid water

- accumulation in a PEMFC with dead-ended anode,” *J. Electrochem. Soc.*, **155**(11), pp. B1168-B1178.
- [7] Raiser, C.A., Bregoli, L., Patterson, T.W., Yi, J.S., Yang, J.D., Perry, M.L., Jarvi, T.D., 2005, “A reverse-current decay mechanism for fuel cells,” *Electrochem Solid-State Lett.*, **8**(6), pp. A1432-1442.
- [8] Siegel, Bohac, S.V., D.A., Stefanopoulou, Yesilyurt, S., 2010, “Nitrogen front evolution in purged polymer electrolyte membrane fuel cell with dead-ended anode” *J. Electrochem. Soc.*, accepted.
- [9] Bird, R.B., Stewart, W.E., Lightfoot, E.N., 2002, *Transport Phenomena*, 2<sup>nd</sup> ed, Wiley, New York.
- [10] Fluckiger, R., Freunberger, S.A., Kramer, D., Wokaun, A., Scherer, G.G., Buchi, F.N., 2008, “Anisotropic, effective diffusivity of porous gas diffusion layer materials in PEFC,” *Electrochimica Acta*, **54**, pp. 551-559.
- [11] Barbir, F., 2005, *PEM Fuel Cells: Theory and Practice*, Academic Press.
- [12] Newman, J., Thomas-Alyea K.E., 2004, *Electrochemical Systems*, 3<sup>rd</sup> ed. John Wiley & Sons, New Jersey, USA.
- [13] Katsounis, A., Balomenou, S.P., Tsiplakides, D., Tsampas, M., Vayenas C.G., 2005, “The role of potential-dependent electrolyte resistance in the performance, steady-state multiplicities and oscillations of PEM fuel cells: Experimental investigation and macroscopic modeling,” *Electrochimica Acta*, **50**, pp. 5132-5143.
- [14] Springer, T.E., Zawodzinski, T.A., and Gottesfeld, S., 1991, “Polymer electrolyte fuel cell model”, *J. Electrochem. Soc.*, **138**(8), 2334-2342.
- [15] Ge, S., Li, X., Yi, B., Hsing, I-M., 2005, “Absorption, desorption, and transport of water in polymer electrolyte membranes for fuel cells,” *J. Electrochem. Soc.*, **152**(6), A1149-A1157.
- [16] COMSOL, 2008, “COMSOL Multiphysics User Guide”, COMSOL A.B., Stockholm.